

HYDRODYNAMIC ANALYSIS OF A SEMI-SUBMERSIBLE FLOATING WIND TURBINE. NUMERICAL VALIDATION OF A SECOND ORDER COUPLED ANALYSIS

Gutiérrez-Romero JE*, Serván-Camas B[†] and García-Espinosa J[†].

*Escuela Técnica Superior de Ingeniería Naval y Oceánica (ETSINO)
Universidad Politécnica de Cartagena
Paseo Alfonso XIII, n 52, 30203
e-mail: jose.gutierrez@upct.es, web page: <http://www.upct.es>

[†] International Center for Numerical Methods in Engineering (CIMNE)
Universidad Politécnica de Cataluña
Edificio C1, Campus Norte UPC
Gran Capitán s/n, 08034 Barcelona, Spain
e-mail: bservan@cimne.upc.edu - Web page: <http://www.cimne.com>

Key words: Seakeeping, Second-order analysis, semisubmersible platform

Abstract. This work presents a comprehensive computational hydrodynamic analysis of a semisubmersible offshore wind turbine. The studied case is based on a three floater wind turbine designed for a 1.5 MW turbine. The analysis is supported by experimental tests and it is focused on the second-order response of the platform, including mooring effects. The different analysis carried out include decay test, regular waves and bichromatic waves. Numerical simulations are performed in time-domain using the computational model implemented in the SeaFEM solver.

The analysis of the obtained results includes the comparison of the numerical and experimental response of the platform. Special attention is paid to the second-order effects in the dynamic response of the system.

1 INTRODUCTION

There is a growing focus of the industry on Floating Offshore Wind Turbines (FOWT) for due to their ability to access the enormous wind resources available over deep water. Despite the existence of real scale prototypes already operating, such as the Hywind in Norway [1] or the Windfloat in Portugal [2], the industry still faces design and operation challenges which require the complete full coupled analysis of them. In this work, we present a full hydrodynamic coupled analysis for the HiPRWind semisubmersible [3] floating wind turbine model using up-to-second-order wave model coupled with non-linear finite element model for mooring analysis, which is validated with experimental tests carry out at ECN Nantes facilities.

The hydrodynamics of the semisubmersible concept for FOWTs has received some attention in the recent literature. For instance, [4] and [5] focused on slow-drift and mean-drift forces

of semisubmersible platforms, a comparison of a semisubmersible against a SPAR concept can be found in [6] and Simulations in the Time-Domain (TD) considering different models for the hydrodynamic loads were carried out in [7].

One of the main concerns regarding semisubmersible platforms are the slow-drift forces. These forces are usually in the range of the surge natural period of semisubmersible platform with catenary mooring lines, leading to large displacements when excited near the resonance frequency. And although the wave frequencies are usually larger than the natural periods, second-order effects contain low frequencies components that will probably excite slow-drift in the system platform-mooring. Therefore, large excursion might happen due to second-order effects.

Second-order forces might increase the surge response of semisubmersible platforms, even becoming larger than the first-order response. And although Neumann's approximation could be used for estimating the slow-drift forces (which only depends on the first-order solution), it might not be enough precise as shown in [5]. Hence, second-order effect must be taken into account to accurately compute slow-drift motions, and design the mooring system accordingly. The impact of the slow-drift forces on the design of the mooring systems and the difficulties to estimate the corresponding forces is yet a problem that requires substantial research. Previous works as López-Pavón et al. [5] putted the focus on the estimation and verification of the second-order wave induced forces on the HiPRWind semisubmersible platform.

So, in this work, a Finite Element Method (FEM) that solves up to second-order in the time-domain model coupled with non-linear forces arising from the mooring lines are used to carry out a hydrodynamic analysis of semisubmersible HiPRWind platform [3, 5]. A verification of the model is carried out comparing to second-order analytical solutions available. The computer model of the HiPRWind platform is calibrated using decay tests and then analyzed in regular and bichromatic. Finally, some conclusions are made regarding the verifications and analysis presented.

2 PROBLEM STATEMENT

Then the problem statement about seakeeping of offshore structures is established. A brief descriptions about second-order and mooring model employed are established.

2.1 Second-order diffraction-radiation governing equations

The governing equations for the second-order diffraction-radiation wave problem are obtained applying Taylor expansion on the boundary surfaces of a time-independent domain. This approach allows to approximate the free surface on $z = \zeta$ and the mean body surface Γ_b^0 at time t . Then, a perturbed solutions based on Stokes expansion procedure is applied to the velocity potential, free surface elevation, and body motion. More details can be found in [8, 9]. The solution can be decomposed as

$$\varphi = \psi + \theta, \quad (1)$$

$$\xi = \eta + \zeta, \quad (2)$$

where ψ is the incident wave velocity potential, θ is the diffraction-radiation wave velocity

potential, η is the incident wave elevation, and ζ is the diffraction-radiation wave elevation. Then, the wave diffraction-radiation governing equations up to second-order are [8, 9]:

$$\Delta\theta^{1+2} = 0 \quad \text{in } \Omega, \quad (3)$$

$$\begin{aligned} \frac{\partial\eta^{1+2}}{\partial t} - \frac{\partial\theta^{1+2}}{\partial z} &= -\frac{\partial\theta^1}{\partial x}\frac{\partial\eta^1}{\partial x} - \frac{\partial\theta^1}{\partial y}\frac{\partial\eta^1}{\partial y} \\ -\frac{\partial\theta^1}{\partial x}\frac{\partial\zeta^1}{\partial x} - \frac{\partial\theta^1}{\partial y}\frac{\partial\zeta^1}{\partial y} &- \frac{\partial\psi^1}{\partial x}\frac{\partial\eta^1}{\partial x} - \frac{\partial\psi^1}{\partial y}\frac{\partial\eta^1}{\partial y} \quad \text{on } z = 0 \end{aligned} \quad (4)$$

$$\begin{aligned} \frac{\partial\theta^{1+2}}{\partial t} + \frac{P_{fs}}{\rho} + g\eta^{1+2} &= -\eta^1\frac{\partial}{\partial z}\left(\frac{\partial\theta^1}{\partial t}\right) - \zeta^1\frac{\partial}{\partial z}\left(\frac{\partial\theta^1}{\partial t}\right) \\ -\eta^1\frac{\partial}{\partial z}\left(\frac{\partial\psi^1}{\partial t}\right) - \frac{1}{2}\nabla\theta^1 \cdot \nabla\theta^1 - \nabla\psi^1 \cdot \nabla\theta^1 &\quad \text{on } z = 0, \end{aligned} \quad (5)$$

$$\mathbf{v}_\theta^{1+2} \cdot \mathbf{n}^1 = -\left(\mathbf{v}_b^{1+2} + \mathbf{v}_\psi^{1+2} + \mathbf{r}_b^1 \cdot (\nabla\mathbf{v}_\theta^1 + \nabla\mathbf{v}_\psi^1)\right) \cdot \mathbf{n}^1 \quad \text{on } \Gamma_b, \quad (6)$$

$$\begin{aligned} \frac{P_b^{1+2}}{\rho} &= -gz_b - g\mathbf{r}_b^{1+2} - \frac{\partial\theta^{1+2}}{\partial t} - \mathbf{r}_b^1 \cdot \nabla\left(\frac{\partial\theta^1}{\partial t}\right) \\ -\frac{1}{2}\nabla\theta^1 \cdot \nabla\theta^1 - \nabla\psi^1 \cdot \nabla\theta^1 &\quad \text{on } \Gamma_b, \end{aligned} \quad (7)$$

where superscripts 1 and 1 + 2 denote the components at the first-order and up to second-order solution, and r_b is the displacement vector at a point over body.

2.2 Body Dynamics

The body dynamics of the floating body are governed by the equation of motion:

$$\bar{\bar{\mathbf{M}}}\mathbf{X}_{tt} + \bar{\bar{\mathbf{K}}} = \mathbf{F}, \quad (8)$$

where $\bar{\bar{\mathbf{M}}}$ is the mass matrix of the body, $\bar{\bar{\mathbf{M}}}$ is the hydrostatic restoring coefficient matrix, \mathbf{F} is the vector of the hydrodynamic forces induced by dynamic pressures plus any other external forces, and \mathbf{X} represent the movements of the six degrees of freedom of the body.

Loads acting on the body are obtained by direct pressure integration on the body surface underneath the mean water level, except for the hydrostatic forces, which are obtained via the corresponding hydrostatic restoring matrices. Also, the second-order loads and moments (\mathbf{F}_{wl}^2 and \mathbf{M}_{wl}^2) due to the change of the wetted surface induced by the first order solution are accounted for:

$$\mathbf{F}_{wl}^2 = -\frac{1}{2}\rho g \int_{\Gamma_{wl}^0} (\xi^1 - r_{pz}^1)^2 \frac{\mathbf{n}_p^0}{\sqrt{1 - (n_{pz}^0)^2}} \quad (9)$$

$$\mathbf{M}_{wl}^2 = -\frac{1}{2}\rho g \int_{\Gamma_{wl}^0} (\xi^1 - r_{pz}^1)^2 \mathbf{G}^0 \vec{\mathbf{P}}^0 \times \frac{\mathbf{n}_p^0}{\sqrt{1 - (n_{pz}^0)^2}} \quad (10)$$

where Γ_{wl}^0 is the mean wetted surface, ξ is the free surface elevation, \mathbf{n}_p is the initial body surface normal vector at point P located on wet surface, $\mathbf{G}^0\vec{\mathbf{P}}^0$ is the vector from the center of gravity of the floater G to any point P on the wet surface. Details of each component can be found in [8, 9].

2.3 Equations for cable dynamics

The dynamic equations for a mooring cable with length L with negligible bending and torsional stiffness can be formulated as [10]

$$(\rho_w C_m A_0 + \rho_0) \frac{\partial^2 \mathbf{r}_l}{\partial t^2} = \frac{\partial}{\partial l} \left(E A_0 \frac{e}{e+1} \frac{\partial \mathbf{r}_l}{\partial l} \right) + \mathbf{f}(t) (1+e), \quad (11)$$

where ρ_w is the water density, C_m is the added mass coefficient, ρ_0 is the mass per unit length of the unstretched cable, \mathbf{r}_l is the position vector, E is the Young's modulus, A_0 is the cross-sectional area of the cable, e is the strain, \mathbf{f} are the external loads applied on the cable, and l is the length along the unstretched cable. The external loads acting on the cable, considered in this work, are the self-weight of the cable, hydrostatic loads, drag forces, and seabed interaction.

3 ANALYSIS OF HIPRWIND FLOATING WIND TURBINE

3.1 Introduction

The floating platform geometry considered in this work has been provided by the HiPRWind FP7 project [3, 11] and is composed by three buoyant columns connected by bracings. Model tests were carried out at ECN Nantes' facilities. A model built in stainless steel with scale $\lambda = 1/19.8$ was used in the tests (see Figure 1). Table 1 provides the platform particulars in full scale, as well as the water depth considered for this study. The mesh model consists of tetrahedral 643603 elements and 119350 nodes. The Figure 2 shows a caption of the mesh used to carry out the hydrodynamic study.



Figure 1: HiPRwind platform model at wave basin.

Table 1: Main particulars of HiPRWind semisubmersible platform.

Item	Value	
Operation design draft	100.0	m
Depth	15.5	m
Distance between column centres	35.0	Kg
Column diameter	7.0	m
Heave plates diameter	20.0	m
Displacement	2332.0	Tons
Centre of gravity ($x_g; y_g; z_g$)	(0.0; 0.0; -4.46)	m
Number of mooring lines	3	
Stiffness	634	MN
Length	330.0	m
Weight per unit length	1453.90	N/m

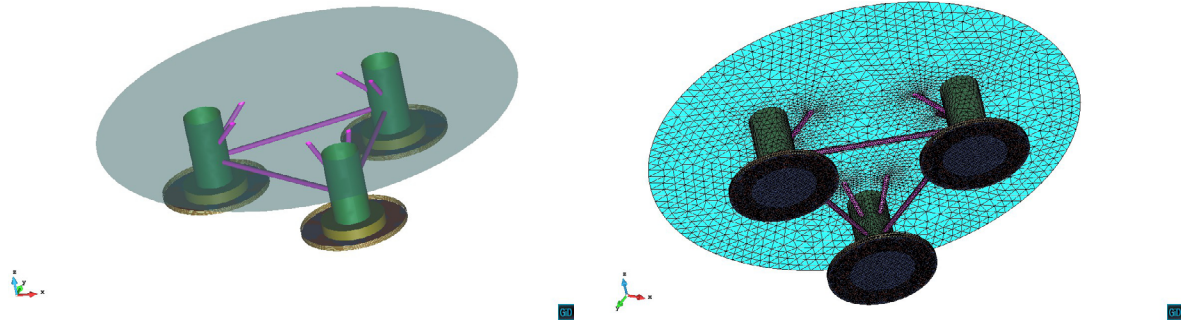


Figure 2: FEM Model and computational mesh overview.

3.2 Calibration of numerical model

In order to predict seakeeping in real conditions with a potential flow solver, viscous effects are to be incorporated via external forces. These external forces are simplified formulas accounting for the overall viscous effects acting on the platform. The viscous effects have been included in the computational solver by means of linear and quadratic damping models. This model has been calibrated using the experimental information of the extinction tests for surge, heave and pitch motions. Three elastic lines were used to keep the position of the model during the extinction experiments. These lines have a small linear weight distribution so the catenary effect is negligible. A pretension of 550 kN were applied to each line.

The viscous damping forces have been divided into two groups. The first group corresponds to the bracings of the structure. The corresponding forces are applied in the center of gravity of the platform. The second group corresponds to the heave plates and columns, and calibration forces are applied in the center of the heave plates assuming a dominant effect of these over the cylinders. Table 2 provides a summary of the coefficients of the damping terms obtained in the

calibration phase.

Table 2: Model calibration: added mass, linear damping and quadratic damping coefficients.

Applied to CG			
Surge linear damping	B_{11}	75	KN(m/s)
Heave added mass	A_{33}	1200	Tn
Heave linear damping	B_{33}	110	KN(m/s)
Applied at the center of heave plates			
Heave linear damping	B_{33}	75	KN(m/s)
Heave quadratic damping	B_{33}^2	805	KN(m/s) ²

Figure 3 shows experimental versus numerical results after calibration for the surge, heave, and pitch decay tests. Good agreement has been reached for the three degrees of freedom. The natural periods obtained are 70 s in surge, 19 s in heave and 26 in pitch respectively.

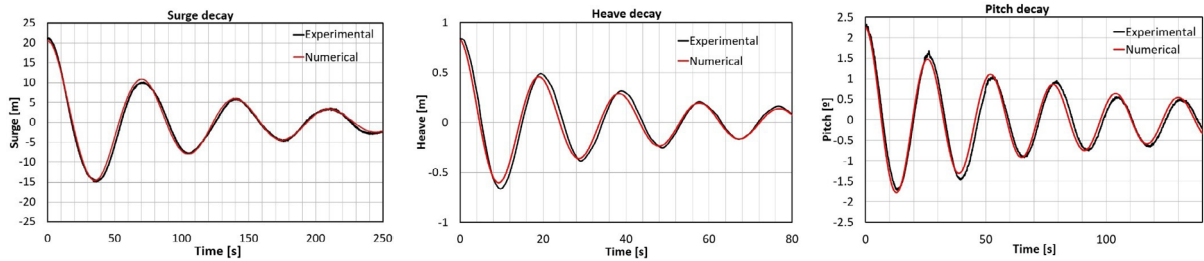


Figure 3: Comparison between experimental and numerical decay tests.

3.3 Regular waves

Once the model has been calibrated against decay test the Response Amplitude Operators (RAOs) of the computational model are obtained and compared with those obtained in the experiments. Three catenary lines were used as mooring lines for the rest of the experiments. Mooring line particulars are given in Table 1.

It has to be said that the experimental data shows a change in the platform response along the experiment, it is to say, the results of the spectral analysis depend on the time interval used. If the period of time used for calculating the RAOs is chosen towards the end of the experiment, an increase of the response in the low frequencies is observed which has raised the concern on whether longer waves are being dissipated appropriately by the beach located at the opposite end of the wave maker. Experimental RAOs were obtained for an equivalent wave height of $H = 2$ m. Figure 5 compares the RAOs in surge, heave, and pitch, respectively, against the numerical results. A good agreement has been found for the three degrees of freedom.

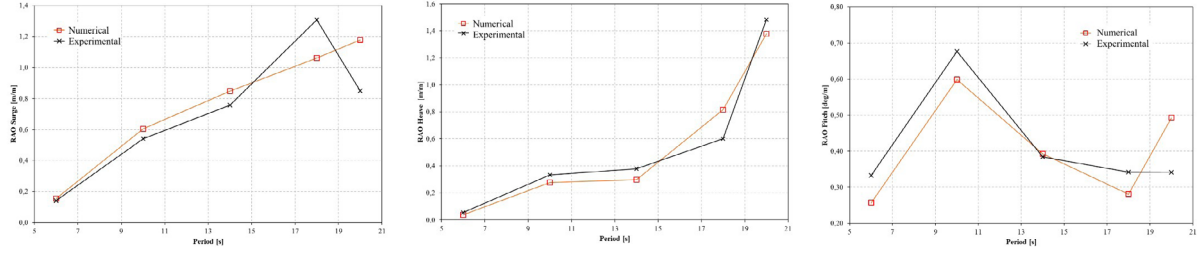


Figure 4: Comparison between experimental and numerical decay tests.

3.4 Bichromatic waves

A number of tests were carried out with bichromatic waves in order to analyze the second-order response of the platform. The incident wave periods range between 5.5 and 21 seconds, corresponding to wave lengths between 47 and 689 meters. The wave frequency difference ranges from 0.0145 Hz to 0.0152 Hz. The latter frequency is close, on purpose, to the surge resonant frequency since the focus of the analysis will be on the surge response to the slow drift.

Table 3 provides the experimental test matrix, including incident wave height (H), length (λ) and period of the two incident waves (T). All these cases have been simulated in the time-domain solver. Once the simulations were carried out, the time series have been transformed to the frequency domain in order to make easier the comparison of the results with the experimental data. Sampling frequency has been adjusted so that the incident wave frequencies, as well as the difference and the sum, are precisely captured by the results of the Fast Fourier Transform (FFT) analysis.

Table 3: Bichromatic wave test.

Case	Incident wave 1			Incident wave 2		
	T_1	H_1	λ_1	H_2	T_2	λ_1
1	3.44	689	21	6.03	402	16
2	2.82	564	19	5.16	344	14.9
3	5.64	564	19	5.16	344	14.9
4	5.63	450	17	4.32	288	13.6
5	5.27	351	15	3.54	236	12.3
6	2.83	189	11	2.1	140	9.5
7	1.88	94	7.8	1.14	76	7
8	1.67	84	7.3	1.02	68	6.6
9	1.35	67	6.6	0.84	56	6
10	1.22	61	6.2	0.77	51	5.7
11	1.11	55	6	0.7	47	5.5

A comparison of the platform movements between the experimental data with the numerical results obtained in this work is given in Figures 5, 6, 7. These figures show the movement

amplitude obtained by applying FFT analysis to time domain response. Very good agreement is found in the incident wave frequencies, which basically correspond to first-order response. Regarding to second-order response, a good agreement is also found between the numerical and experimental results, as well as for the rest of frequencies. In fact, the numerical results follow quite well the experimental trends. It has to be mentioned that measuring second-order response in experiments is a tough task, and can easily introduce uncertainties in the final results.

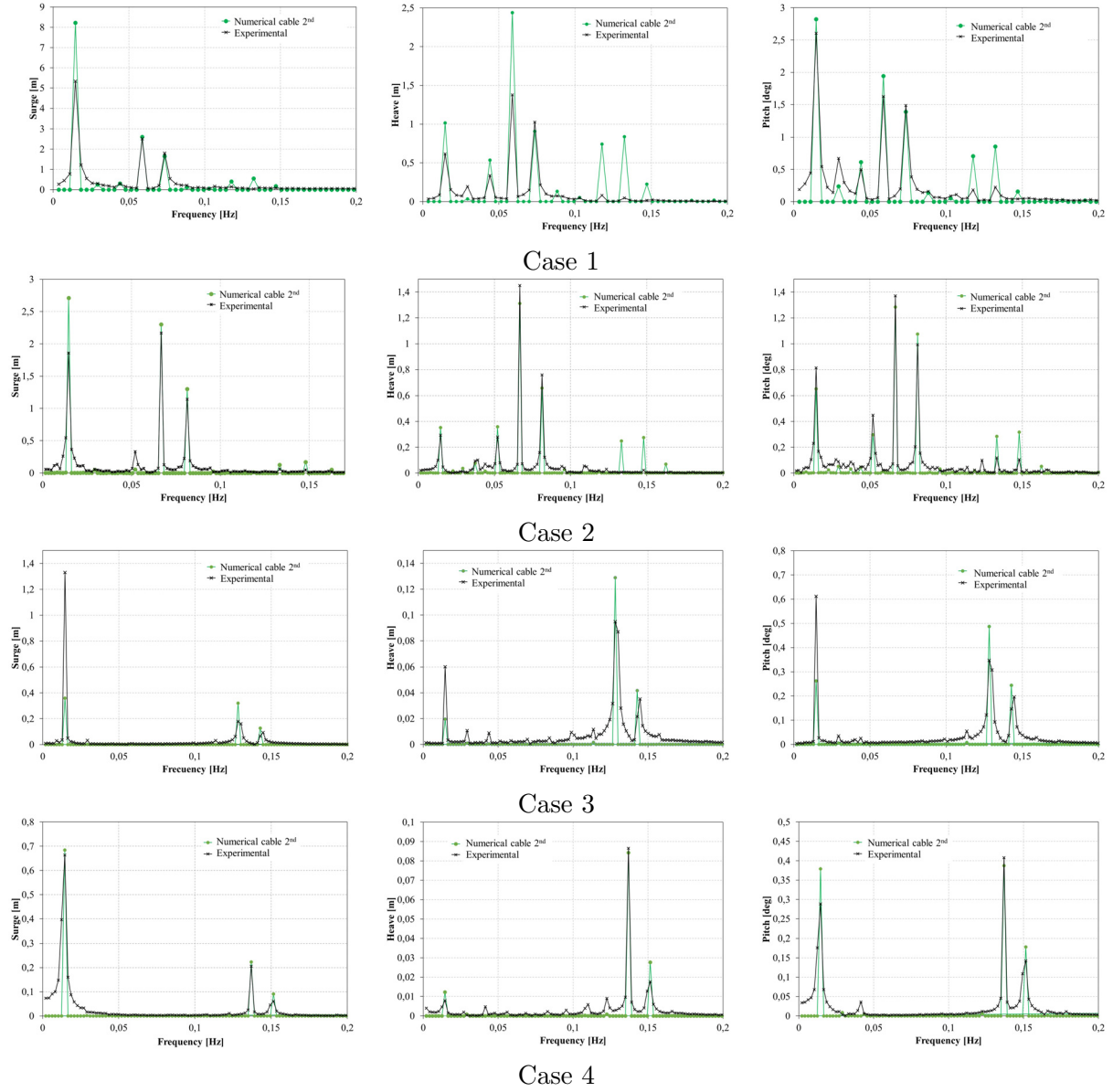


Figure 5: Case 1, 2, 3 and 4. Pitch (on the right), heave and surge (on the left) response amplitudes.

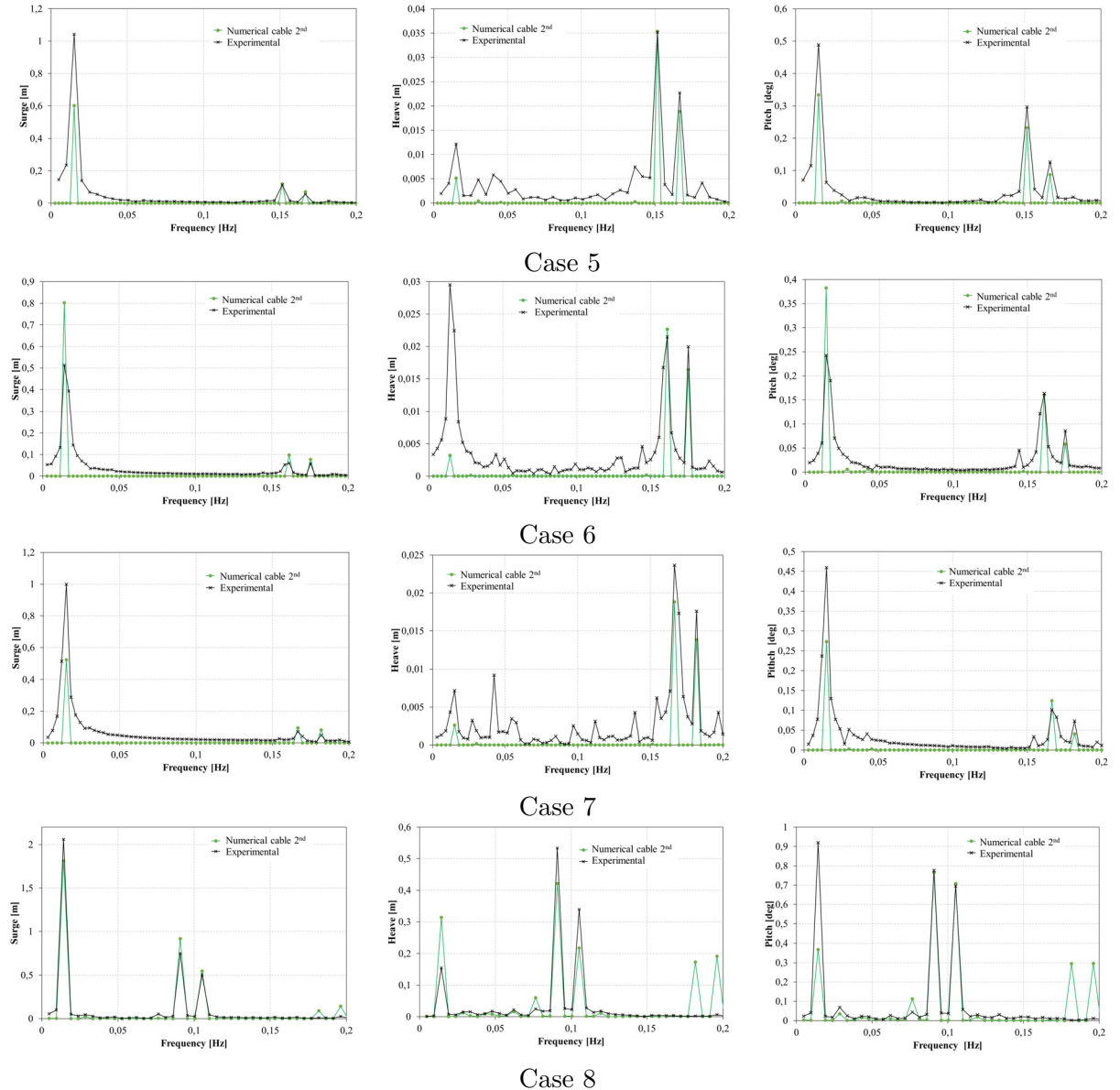


Figure 6: Case 5, 6, 7 and 8. Pitch (on the right), heave and surge (on the left) response amplitudes.

Figure 8 compares the experimental and numerical tensions registered at the fairlead point for the line 1. This mooring line represent the mooring line aligned with the direction of wave propagation. The lines 2 and 3 are placed in a symmetric configuration respect to the wave direction. Since numerical simulation were carried out without sway, roll, and yaw due to the symmetry of the problem), numerical results for mooring lines 2 and 3 are the same. The results are not relevant compared with line 1. The experimental measurements of the fairlead mooring tension and the values obtained from the numerical simulation tensions compare well considering

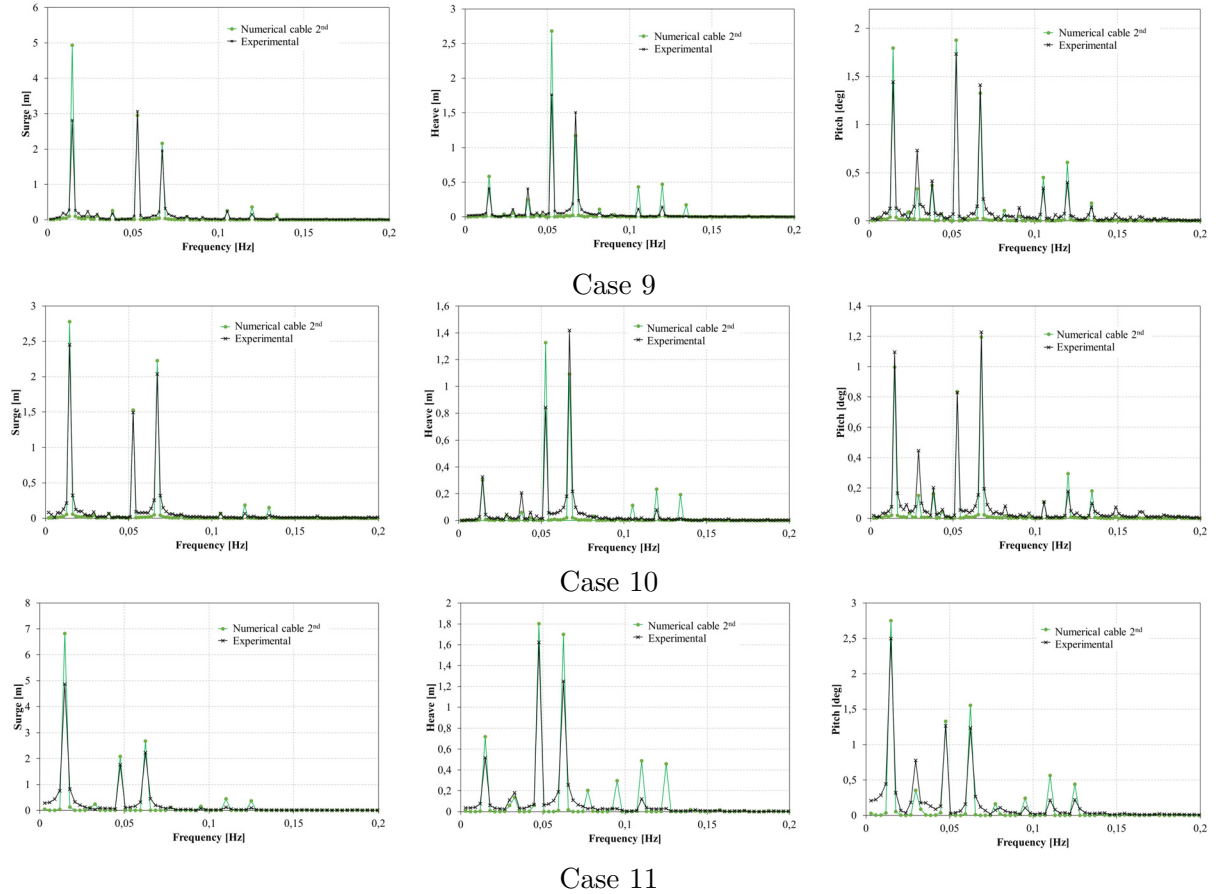


Figure 7: Case 9, 10 and 11. Pitch (on the right), heave and surge (on the left) response amplitudes.

all the uncertainties of the experiment, as well as the difficulty of measuring second-order effects. Looking at the numerical results in Figure 8, it is observed that mooring model provide very similar results.

4 CONCLUSIONS

A FEM model for the second-order wave diffraction-radiation problem in the time-domain has been validated against experiments carried out at the ECN Nantes facilities for the HiPRWind model. In a first stage, the model viscous damping was calibrated to reproduce decay tests for surge, heave, and pitch. A good match between the experiments and the calibrated model was obtained. Then, RAOs were compared using the monochromatic wave tests, finding that the numerical results follow well the trend of the experiments. Finally, simulation of the platform subject to bichromatic waves were performed and compared to the experiments. Taking into account the experimental uncertainties associated to measuring second-order quantities, it has been found that the computed movements of the platform reproduced well the experimental data.

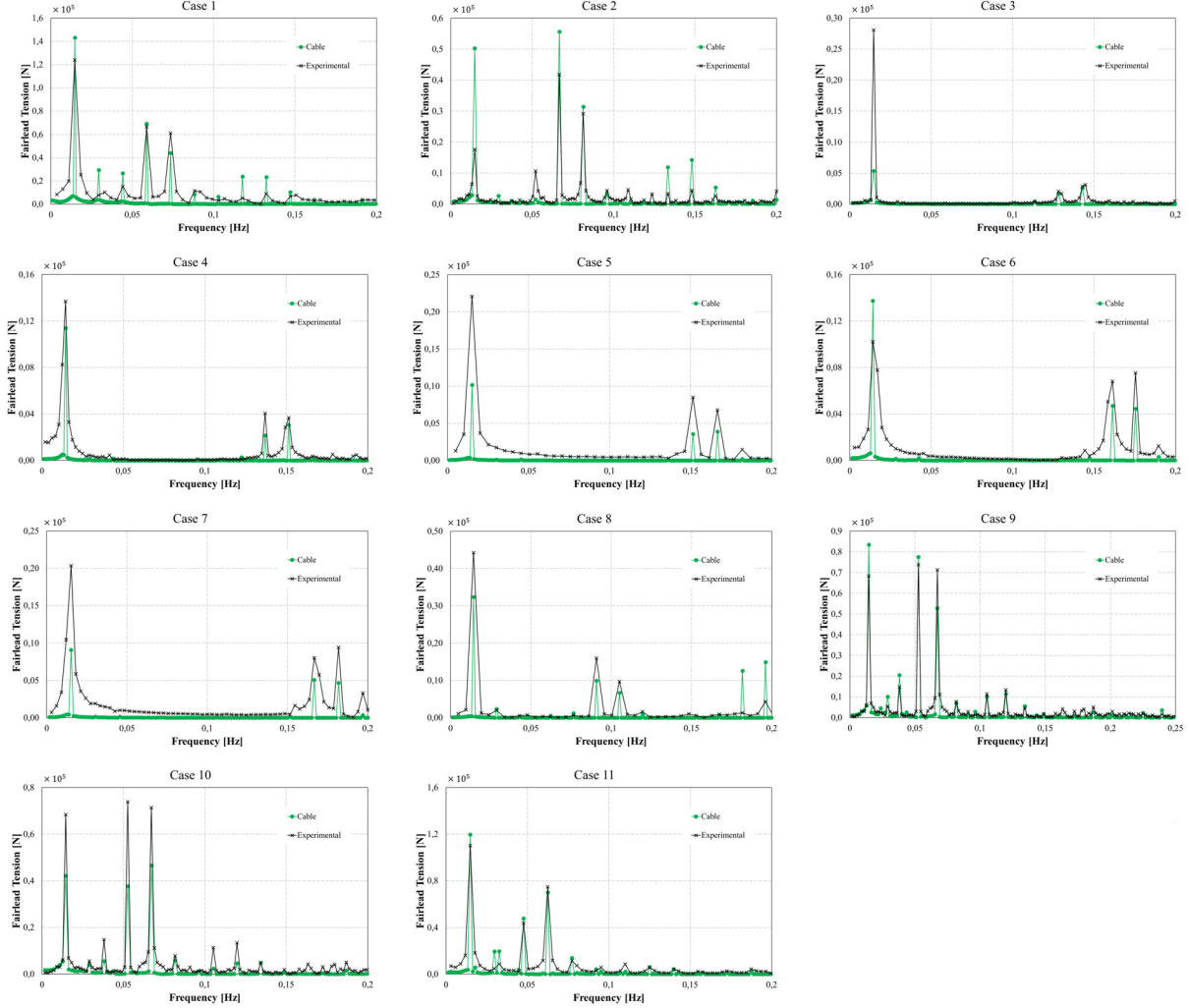


Figure 8: Comparison of mooring line 1 tension at fairlead point for all cases.

Regarding the modeling of the mooring lines, the obtained results agree well with the experimental trends. They also indicate that for the operational conditions analyzed in this work the nonlinear FEM dynamic cable provides quite similar results. In conclusion, the second-order time-domain FEM model along with the nonlinear mooring model has been proven to successfully solve the second-order movements of the HiPRWind platform. In particular, under bichromatic waves designed to enhance slow-drift problem in surge.

5 ACKNOWLEDGEMENTS

The authors acknowledge ECN Nantes which facilities made this work possible. The authors thank A.N. Simos, F. Ruggeri, R. Watai, A. Souto-Iglesias and C. Lopez-Pavon for providing the experimental results for the semi-submersible floater. Thanks also to Acciona Energía and Fraunhofer Institute, and especially to Raul Manzanas. The research leading to these results

has received funding from the Spanish Ministry for Economy and Competitiveness under Grants ENE2014-59194-C2-1-R and ENE2014-59194-C2-2-R (X-SHEAKS). The authors also gratefully acknowledge the support of NVIDIA Corporation with the donation of a TeslaK20 GPU used for this research.

REFERENCES

- [1] Hanson, T.D. Skaare, B. Yttervik, R. Nielsen, F.G. and Havmoller, O. Comparison of Measured and Simulated Responses at the First Full Scale Floating Wind Turbine HYWIND. EWEA 2011, European Wind Energy Association, Brussels, Belgium. (2011).
- [2] Roddier, D. Cermelli, C. Aubault, A. and Weinstein, A. Windfloat: A Floating Foundation for Offshore Wind Turbines. *J. Renewable Sustainable Energy* (2010) **2**(3):033104.
- [3] Simos, A.N. Ruggeri, F. Watai, R. Souto-Iglesias, A. and Lopez-Pavon, C. Slow-drift of a Floating Wind Turbine: An Assessment of Frequency-Domain Methods based on Model Tests (2017) (submitted for publication).
- [4] Lupton, R.C. and Langley, R.S. Scaling of slow-drift motion with platform size and its importance for floating wind turbines. *Renewable Energy* (2017) **101**:1013–1020.
- [5] López-Pavón, C. Watai, R.A. Ruggeri, F. Simos, A.N. and Souto-Iglesias, A. Influence of Wave Induced Second-Order Forces in Semisubmersible FOWT Mooring Design. *Journal of Offshore Mechanics and Arctic Engineering* (2015) **137**/ 031602–1.
- [6] Peiffer, A. Aubault, A. and Weinstein, J. A Generic 5 MW Windfloat for Numerical Tool Validation and Comparison Against a Generic Spar. *ASME Paper No. OMAE* (2011) 50278.
- [7] Philippe, M. Babarit, A. and Ferrant, P. Aero-Hydro-Elastic Simulation of a Semi-Submersible Floating Wind Turbine. *ASME Paper No. OMAE* (2012) 84070.
- [8] Serván-Camas, B. and García-Espinosa J. Accelerated 3D multi-body seakeeping simulations using unstructured finite elements. *J Comput Phys* (2013) **252**:382e403.
- [9] Serván-Camas B. A time-domain finite element method for seakeeping and wave resistance problems. (Doctoral thesis). School of Naval Architecture and Ocean Engineering, Technical University of Madrid. (2016).
- [10] Gutiérrez-Romero, J.E. Serván-Camas, B. García-Espinosa, J. and Zamora-Parra, B. Non-linear dynamic analysis of the response of moored floating structures. *Marine Structures* 2016 **49**:116–137.
- [11] <http://hiprwind.eu/>.